

A Galactic Plane Defined by the Milky Way H II Region Distribution

L. D. ANDERSON,^{1,2,3} TREY V. WENGER,⁴ W. P. ARMENTROUT,^{1,3,5} DANA S. BALSER,⁶ AND T. M. BANIA⁷

¹*Department of Physics and Astronomy, West Virginia University, Morgantown WV 26506, USA*

²*Adjunct Astronomer at the Green Bank Observatory, P.O. Box 2, Green Bank WV 24944, USA*

³*Center for Gravitational Waves and Cosmology, West Virginia University, Chestnut Ridge Research Building, Morgantown, WV 26505, USA*

⁴*Astronomy Department, University of Virginia, P.O. Box 400325, Charlottesville, VA 22904-4325, USA*

⁵*Green Bank Observatory, P.O. Box 2, Green Bank WV 24944, USA*

⁶*National Radio Astronomy Observatory, 520 Edgemont Road, Charlottesville VA, 22903-2475, USA*

⁷*Institute for Astrophysical Research, Department of Astronomy, Boston University, 725 Commonwealth Ave., Boston MA 02215, USA*

ABSTRACT

We develop a framework for a new definition of the Galactic midplane, allowing for tilt (θ_{tilt} ; rotation about Galactic azimuth 90°), and roll (θ_{roll} ; rotation about Galactic azimuth 0°) of the midplane with respect to the current definition. Derivation of the tilt and roll angles also determines the solar height above the midplane. Here we use nebulae from the *WISE* Catalog of Galactic H II Regions to define the Galactic high-mass star formation (HMSF) midplane. We analyze various subsamples of the *WISE* catalog and find that all have Galactic latitude scale heights near 0.30° and z -distribution scale heights near 30 pc. The vertical distribution for small (presumably young) H II regions is narrower than that of larger (presumably old) H II regions (~ 25 pc versus ~ 40 pc), implying that the larger regions have migrated further from their birth sites. For all H II region subsamples and for a variety of fitting methodologies, we find that the HMSF midplane is not significantly tilted or rolled with respect to the currently-defined midplane, and therefore the Sun is near to the HMSF midplane. These results are consistent with other studies of HMSF, but are inconsistent with many stellar studies, perhaps due to asymmetries in the stellar distribution near the Sun. Our results are sensitive to latitude restrictions, and also to the completeness of the sample, indicating that similar analyses cannot be done accurately with less complete samples. The midplane framework we develop can be used for any future sample of Galactic objects to redefine the midplane.

Keywords: Galaxy: structure – ISM: H II regions

1. INTRODUCTION

The midplane, the plane at Galactic latitude $b = 0^\circ$, was defined in 1958 by the IAU subcommission 33b, which set the Galactic coordinate system (Blaauw et al. 1960). The IAU midplane definition comes from the Galactic Center location in B1950 coordinates of (17:42:26.6, $-28:55:00$) and the north Galactic pole location in B1950 coordinates of (12:49:00, $+27:24:00$). Ideally, the midplane definition would contain the minimum of the Galactic potential and there would be equal amounts of material above and below the midplane. The vertical distribution of objects with respect to the Galactic midplane tells us fundamental parameters of Galactic structure, such as the scale height of the objects studied, the Sun’s height above or below the midplane, z_\odot , and even the orientation of the midplane itself. Nearly all previous studies of the vertical distribution of objects in

the Galaxy have found an asymmetry in the distribution of sources above and below the plane, with more sources found below the IAU plane than above it. This asymmetry is generally assumed to be the result of the Sun’s location above the IAU Galactic midplane.

Previous studies of the vertical distribution of objects and solar height above the plane can be categorized as either using stellar or gas samples. Solar height studies are summarized in Humphreys & Larsen (1995) and Karim & Mamajek (2017). Studies of stellar samples have a long history; perhaps the first such study was done by van Tulder (1942), who found an asymmetry in the stellar distribution that implied that the Sun is 14 ± 2 pc above the plane. Typical stellar studies examine discrepancies in the number of sources toward the north and south Galactic poles to determine the solar height (e.g., Humphreys & Larsen 1995). A typical

Table 1. Previous Results Analyzing the b and z -Distributions of Galactic Objects

Tracer	Galactic Latitude b		Height z		Zone	Reference ^b
	Scale Height ^a (deg.)	Peak (deg.)	Scale Height ^a (pc)	Peak (pc)		
ATLASGAL 870 μm cont.	0.3	-0.076 ± 0.008			$-60^\circ < \ell < 60^\circ; b \leq 1.5^\circ$	1
ATLASGAL 870 μm cont.			28 ± 2	-6.7 ± 1.1	$-60^\circ < \ell < 60^\circ; b \leq 1.5^\circ$	2
ATLASGAL 870 μm cont.			31 ± 3	-4.1 ± 1.7	$-60^\circ < \ell < 0^\circ; b \leq 1.5^\circ$	2
ATLASGAL 870 μm cont.			24 ± 1	-10.3 ± 0.5	$0^\circ < \ell < 60^\circ; b \leq 1.5^\circ$	2
BGPS 1.1 mm cont.		-0.095 ± 0.001			$-10^\circ < \ell < 90.5^\circ; b < 0.5^\circ$	3
BGPS 1.1 mm cont.			27 ± 1	-9.7 ± 0.6	$15^\circ < \ell < 75^\circ; b < 0.5^\circ$	4 ^c
IR-identified star clusters	0.66 ± 0.07				Entire Galaxy	5
Ultra-compact HII regions					Entire Galaxy	6
Ultra-compact HII regions			31		$-10^\circ < \ell < 40^\circ; b \leq 0.5^\circ$	7
Ultra-compact HII regions	0.6		30		Entire Galaxy	8
HII regions			42	-11	$17.9 < \ell < 55.4^\circ; b < 1^\circ$	9
HII regions			39.3	-7.3	Entire Galaxy, $R_{\text{Gal}} < R_0$	10 ^d
HII regions			33.0 ± 0.06	-7.6	Entire Galaxy, $R_{\text{Gal}} < R_0$	11 ^e
High mass star forming regions			29 ± 0.5	-20 to 0	$17.9 < \ell < 55.4^\circ; b < 1^\circ$	12
CH ₃ OH masers	0.4 ± 0.1				$-174^\circ < \ell < 33^\circ$	13
HI cold neutral medium			~ 150		Entire Galaxy	14
CO	0.45				Entire Galaxy	15
Far-IR dust	0.50				Entire Galaxy	16
Far-IR dust	0.32	-0.06			$-70^\circ < \ell < 68^\circ; b < 1.0^\circ$	17
158 μm [CII]	0.56		73	-28	Entire Galaxy at $b = 0^\circ$	18

^aAs listed in the paper, regardless of whether value corresponds to the exponential or Gaussian scale height (see Equation 1).

^b1: Beuther et al. (2012); 2: Wienen et al. (2015); 3: Rosolowsky et al. (2010); 4: Ellsworth-Bowers et al. (2015); 5: Mercer et al. (2005); 6: Bronfman et al. (2000); 7: Becker et al. (1994); 8: Wood & Churchwell (1989); 9: Anderson & Bania (2009); 10: Paladini et al. (2004); 11: Bobylev & Bajkova (2016); 12: Urquhart et al. (2011); 13: Walsh et al. (1997); 14: Kalberla (2003); 15: Dame et al. (1987); 16: Beichman et al. (1988); 17: Molinari et al. (2015); 18: Langer et al. (2014)

^cThese authors correct for the solar offset above the Galactic midplane. Quoted values are our computations from their database, using $z = d_\odot \sin(b)$ and the Brand (1986) rotation curve.

^dValues are only for the sample with the most accurate distances.

^eListed scale height is from the authors' Gaussian model fit.

value for the solar height from stellar studies is 20 pc; for example, Maíz-Apellániz (2001) used OB stars from *Hipparchos* to derive $z_\odot = 24.2 \pm 1.7$ pc, Chen et al. (2001) used stars from an early release of the Sloan Digital Sky Survey (SDSS) to derive $z_\odot = 27 \pm 4$ pc., and Jurić et al. (2008) found using SDSS data release 3 (with some data release 4) that the z -distributions for stars of a range of colors and brightnesses are all consistent with $z_\odot \simeq 25$ pc.

We summarize the studies of Galactic latitude and z -distributions that use gas tracers in Table 1, focusing on works that use tracers sensitive to HMSF. This table contains the peak and scale height of the distributions. If the fits were exponential, we list the stated scale height. If the fits were Gaussians, we list the scale height h as

$$h = \frac{\text{FWHM}}{2(2 \ln 2)^{0.5}}, \quad (1)$$

where FWHM is the full width at half maximum of the distribution. For a given sample, we do not expect significant discrepancies between the exponential and Gaussian scale heights (Bobylev & Bajkova 2016). There are larger discrepancies between values derived using gas tracers compared to those derived using stellar tracers. There is, nevertheless, good agreement that the various distributions peak below the Galactic midplane.

The tracers that are most sensitive to HMSF have narrow distributions with scale heights ~ 40 pc, whereas the distributions of HI, CO, far-infrared emitting dust, and CII are broader.

The solar height above the plane derived using gas tracers is generally lower than that found from stellar tracers (see compilation in Karim & Mamajek 2017). Typical values are near 10 pc. For example, Bobylev & Bajkova (2016) found $z_\odot = 8 \pm 2$ pc from a sample of HII regions, masers, and molecular clouds and Paladini et al. (2003) found $z_\odot = 9.3 \pm 2$ pc using a sample of HII regions.

Because it was defined using low-resolution data and our measurements have since improved significantly, the IAU-defined Galactic midplane may need to be revised (Goodman et al. 2014). We now know that Sgr A* lies at $b = -0.046165^\circ$ (Reid & Brunthaler 2004), which places it below the IAU-defined location of the Galactic Center (although by the IAU's definition Sgr A is at the Galactic center (Blaauw et al. 1960)). Goodman et al. (2014) investigated the implications of this offset and of the Sun lying above the midplane using the extremely long "Nessie" infrared dark cloud (IRDC). Although Nessie lies below the midplane as it is currently defined, because of the Sun's offset and the offset of Sgr A* from

$b = 0^\circ$, they found that Nessie may actually lie in what they call the “true” midplane, which is tilted by angle θ_{tilt} with respect to the IAU midplane definition¹. While suggestive, this study needs to be expanded to a larger sample of objects in order to make stronger claims about the midplane definition.

Tracers of HMSF formation should define the Galactic midplane, although it is difficult to create a large, unbiased sample of HMSF regions. Most of the gas tracers are related to massive stars, which are born in the most massive molecular clouds in the Galaxy. The high-mass stars themselves have lifetimes short enough that they are unable to travel far from their birthplaces. For example, an O-star with a space velocity of 10 km s^{-1} can only travel 100 pc out of the midplane in 10 Myr, and only then if its velocity is entirely in the \hat{z} direction. Other tracers of high-mass stars should be similarly restricted to the midplane.

In Section 2, we first develop the methodology needed to redefine the Galactic midplane. We apply this methodology to the *WISE* Catalog of Galactic H II Regions (Anderson et al. 2014) in Section 4, after first characterizing the vertical structure of the Galaxy’s H II region population in Section 3. We therefore define the HMSF midplane, determine the tilt and roll angles of the HMSF midplane with respect to the current IAU definition and determine the Sun’s displacement from the HMSF midplane. The *WISE* catalog does not suffer from the same incompleteness and biases of other studies, and so may be better suited to determining the HMSF midplane than tracers used previously.

2. DEFINING THE GALACTIC MIDPLANE

Here, we develop the methodology required to define the midplane using a sample of discrete Galactic objects. Although the derived equations are general, we assume in later sections that the midplane passes through Sgr A*. Future analyses with more data points may be able to relax this assumption.

2.1. Coordinate systems

To define the Galactic midplane, we need to use two coordinate systems: the current IAU Galactic coordinate system centered on the Sun (x , y , and z) and a new one centered on Sgr A* (x' , y' , z') using the “modified” midplane definition. A Galactic azimuth (az) of zero degrees connects the Sun and the Galactic Center, and azimuth increases clockwise in the plane as viewed from

¹ We call this rotation the “tilt” angle to be consistent with previous authors, although by convention it would be called the “pitch” angle.

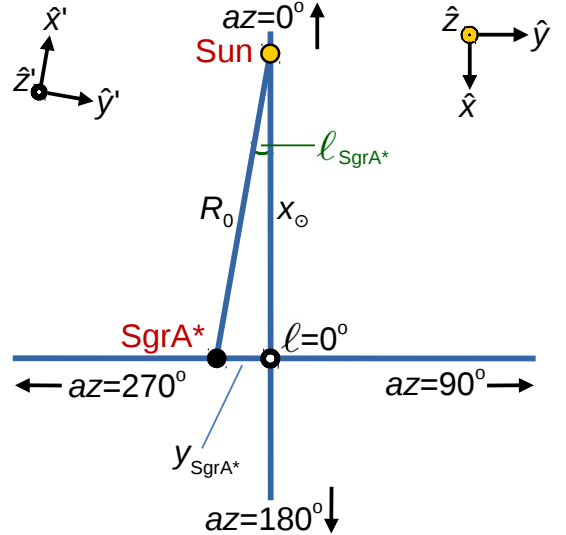


Figure 1. Face-on geometry of the two coordinate systems used here, as viewed from the Galactic north pole (along \hat{z}'). Angles are exaggerated for clarity. Unprimed coordinates are centered on the Sun, whereas primed coordinates are centered at Sgr A*. Angles are indicated with green lines and font. Although \hat{z} is not exactly out of the plane due to the midplane tilt, we ignore this complication when showing the coordinates.

the north Galactic pole.² In the Sun-centered coordinates, \hat{x} points from the Sun to the (currently-defined) Galactic center, \hat{y} points in the direction of Galactic azimuth $az = 90^\circ$, and \hat{z} points toward the Galactic north pole. In the Sgr A*-centered coordinate system, \hat{x}' points from Sgr A* in the approximate direction of the Sun, \hat{y}' points in the direction of Galactic azimuth $az \simeq 90^\circ$, and \hat{z}' points approximately toward the Galactic north pole.

We show the geometries of the two coordinate systems in Figures 1, 2, and 3. The modified midplane can be tilted by angle θ_{tilt} (rotated about \hat{x}' ; Figure 2) and rolled by angle θ_{roll} (rotated about \hat{y}' ; Figure 3). The modified midplane takes the form

$$z' = \theta_{\text{tilt}}(x - x_{\text{SgrA}^*}) + \theta_{\text{roll}}(y - y_{\text{SgrA}^*}) + (z - z_{\text{SgrA}^*}). \quad (2)$$

Sgr A* is located at $(\ell_{\text{SgrA}^*}, b_{\text{SgrA}^*}) = (359.944249^\circ, -0.046165^\circ)$ (Reid & Brunthaler 2004), which gives non-zero values for y_{SgrA^*} and z_{SgrA^*} . As can be seen in Figure 2,

$$z_{\text{SgrA}^*} = R_0 \sin b_{\text{SgrA}^*}. \quad (3)$$

² Technically, az is different between the two coordinate systems. We use here the azimuth defined in the current coordinate system, but only to orient the reader.

We can use the geometries in Figures 1 and 3 to determine

$$y_{\text{SgrA}^*} = \frac{R_0 \sin \ell_{\text{SgrA}^*}}{\cos \theta_{\text{roll}}}. \quad (4)$$

We derive conversions between these coordinate systems in Appendix A, with the main result being the derivation of z' :

$$\begin{aligned} z' = & (R_0 - x) \sin \theta_{\text{tilt}} \cos \theta_{\text{roll}} \\ & - (y_{\text{SgrA}^*} - y) \sin \theta_{\text{roll}} \\ & + (z - z_{\text{SgrA}^*}) \cos \theta_{\text{tilt}} \cos \theta_{\text{roll}} \end{aligned} \quad (5)$$

where

$$\begin{pmatrix} x \\ y \\ z \end{pmatrix} = \begin{pmatrix} d_{\odot} \cos \ell \cos b \\ d_{\odot} \sin \ell \cos b \\ d_{\odot} \sin b \end{pmatrix}. \quad (6)$$

We can therefore compute z' for each Galactic object, given its (x, y, z) values, the rotation angles, and the location of Sgr A*. We give the z -heights for locations along $az = 0^\circ$ in Table 2.

2.1.1. Midplane tilt, midplane roll, and the Sun's height

The tilt angle, which is apparent in Figure 2, does not have a compact analytical form unless we make some simplifying assumptions. Its complete form can be found by solving (cf. Appendix A):

$$\begin{aligned} z'_{\odot} = & R_0 \sin \theta_{\text{tilt}} \cos \theta_{\text{roll}} - y_{\text{SgrA}^*} \sin \theta_{\text{roll}} \\ & + z_{\text{SgrA}^*} \cos \theta_{\text{tilt}} \cos \theta_{\text{roll}}. \end{aligned}$$

To simplify the equation for θ_{tilt} , we assume that $\theta_{\text{tilt}} \simeq 0$ (Goodman et al. 2014, find $\theta_{\text{tilt}} \simeq 0.1^\circ$), so $\cos \theta_{\text{tilt}} \simeq 1$. We can further assume that $\theta_{\text{roll}} \simeq 0$ so that $\cos \theta_{\text{roll}} \simeq 1$ and $y_{\text{SgrA}^*} \sin \theta_{\text{roll}}$ is small compared to the other terms. The tilt angle is then:

$$\theta_{\text{tilt}} \simeq \sin^{-1} \left(\frac{z'_{\odot} + z_{\text{SgrA}^*}}{R_0} \right) \quad (7)$$

This differs from the angle used in Ellsworth-Bowers et al. (2013) by the additional term z_{SgrA^*} .

The roll angle is apparent in Figure 3. There is no compact solution for θ_{roll} under reasonable assumptions. Its full form can be found by solving Equation A6.

3. THE WISE CATALOG OF GALACTIC H II REGIONS

We wish to investigate the HMSF midplane using H II regions in the WISE Catalog of Galactic H II Regions (hereafter the WISE catalog Anderson et al. 2014), which contains all known Galactic H II regions. First, however, we characterize this sample of H II regions, and define subsamples to investigate how results may change

when smaller numbers of H II regions are used. We use V2.1 of the WISE catalog³, which contains 1813 known H II regions that have ionized gas spectroscopic observations, 1130 of which have known distances. This H II region sample extends across the entire Galactic disk to Heliocentric distances > 20 kpc and Galactocentric distances > 18 kpc (Anderson et al. 2015). Since the WISE catalog was derived using $6''$ -resolution $12 \mu\text{m}$ data, or $2''$ Spitzer data in crowded fields, and the nominal H II region size is on the order of arcminutes, confusion is minimal. Therefore, the WISE catalog suffers less from blending of distant regions compared with lower resolution studies (see Beuther et al. 2012). The catalog also has no latitude restriction, which removes an additional impediment to the study of the vertical distribution of HMSF (see Section 4.4.3).

We compute the height above the plane, z , for each WISE catalog H II region using Equation 6:

$$z = d_{\odot} \sin(b), \quad (8)$$

where d_{\odot} is the Heliocentric distance and b latitude from the nominal H II region centroid position in the catalog. The definition of z has no correction for the Sun's height above the midplane, and so differs from that used in some recent studies (e.g., Ellsworth-Bowers et al. 2015). There is also no correction for the displacement of Sgr A* below $b = 0^\circ$.

If available, the catalog distances are from maser parallax measurements (e.g., Reid et al. 2009, 2014), but otherwise they are kinematic distances. The original WISE catalog used the Brand & Blitz (1993, hereafter B93) rotation curve for kinematic distances. Here, we update all known H II region distances using the method of Wenger et al. (2018, hereafter ‘‘MC’’), which better accounts for uncertainties in kinematic distances. Because of their large uncertainties, the catalog contains no kinematic distances for H II regions within 10° in Galactic longitude of the Galactic Center, within 20° of the Galactic anti-center, and for any region where the distance uncertainty is $> 50\%$. We use $R_0 = 8.34$ kpc throughout (Reid et al. 2014).

Because of the Galactic warp, we cannot use all cataloged H II regions to investigate vertical structure in the Galaxy. The warp is known to begin around the solar orbit (Clemens et al. 1988), at $R_0 \simeq 8.34$ kpc. We investigate the warp by plotting the z distribution of H II regions as a function of R_{Gal} in the top panel of Figure 4. Each point in the top panel of Figure 4 represents an H II region, color-coded by its Galactic longitude. In agree-

³ <http://astro.phys.wvu.edu/wise/>

Table 2. Reference points in the two coordinate systems

Location	Sun-centered	Sgr A*-centered
(ℓ, b, d)	z	z'
Sun: $(-, -, 0)$	0	$R_0 \sin \theta_{\text{tilt}} \cos \theta_{\text{roll}} - z_{\text{SgrA}^*} \cos \theta_{\text{tilt}} \cos \theta_{\text{roll}} = z'_{\odot}$
Sgr A*: $(\ell_{\text{SgrA}^*}, b_{\text{SgrA}^*}, R_0)$	$R_0 \sin b_{\text{SgrA}^*} = z_{\text{SgrA}^*}$	0
Current GC: $(0^\circ, 0^\circ, R_0)$	0	$-z_{\text{SgrA}^*} \cos \theta_{\text{tilt}} \cos \theta_{\text{roll}}$

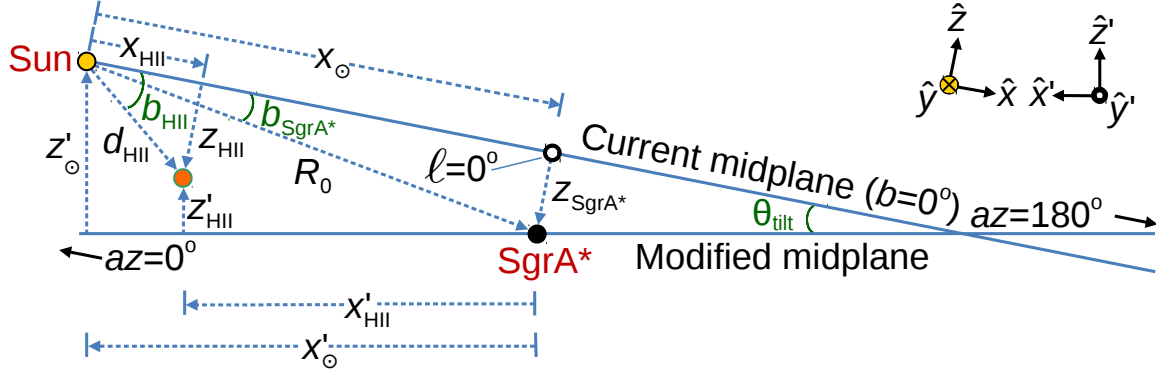


Figure 2. Geometry used for calculations of the midplane tilt rotation angle and the Sun’s height above the plane. Angles are exaggerated for clarity and are indicated with green lines and font. Primed quantities correspond to distances in the coordinate system defined by the modified midplane that passes through Sgr A*. The modified midplane is tilted by an angle θ_{tilt} , for a cut through the plane at Galactic azimuth of 0° as viewed from an azimuth of 270° . One example H II region is shown to represent the analysis done in the next section on the entire H II region population. Although \hat{y} is not exactly out of the plane due to the fact that $\ell_{\text{SgrA}^*} \neq 0$, we ignore this complication when showing the coordinates.

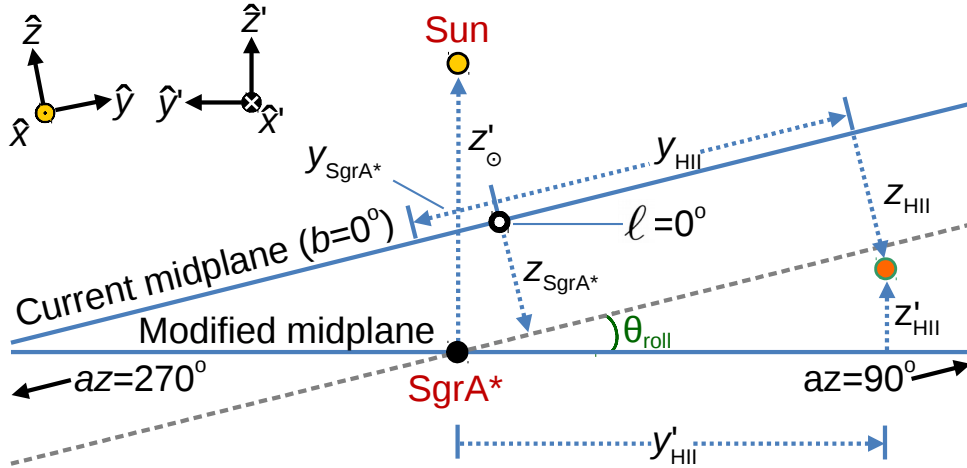


Figure 3. Geometry used for calculations of the roll angle. Angles are exaggerated for clarity and are indicated with green lines and font. Primed quantities correspond to distances in the coordinate system defined by the modified midplane that passes through Sgr A*. We show the geometry for a roll angle θ_{roll} , for a cut through the plane at Galactic azimuth of 90° as viewed from an azimuth of 180° (Sgr A* is in the foreground). The third and fourth Galactic quadrants are therefore on the left of the diagram and the first and second quadrants are on the right. One example object, an H II region, is shown. Although \hat{x} is not exactly out of the plane due to the fact that $\ell_{\text{SgrA}^*} \neq 0$, we ignore this complication when showing the coordinates.

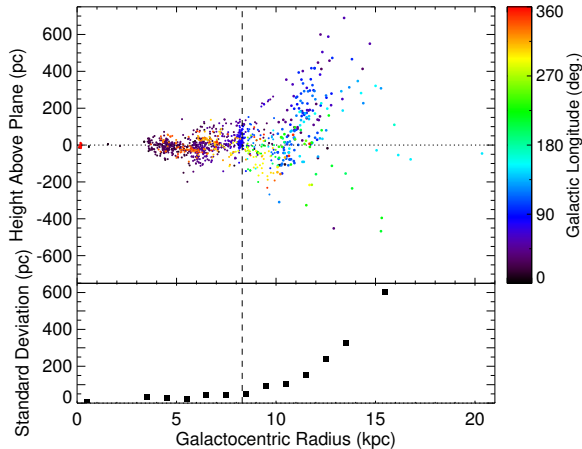


Figure 4. The warping and flaring of the Galactic disk. Shown is the height above the plane relative to IAU definition, z , versus Galactocentric radius R_{Gal} for the H II regions in the sample (top panel). The color of each point corresponds to the Galactic longitude of the region. We decrease the symbol size at low values of R_{Gal} for clarity. The warp begins near the solar circle, $R_{\text{Gal}} \simeq 8.34$ kpc (dashed vertical line), in agreement with previous studies. The warp is toward the North Galactic pole in the first and second quadrants (black/purple/blue points) and toward the South Galactic pole in the third and fourth quadrants (green/yellow/orange points). In the bottom panel, black filled squares show the standard deviation of the z -heights derived from Gaussian fits to sources in 1 kpc bins. Within the solar circle, the standard deviation is $\lesssim 50$ pc, and this can be thought of as the scale height. Outside the Solar circle, the standard deviation increases rapidly due to the Galactic warp.

ment with previous results, the warp as traced by H II regions begins near the solar circle ($R_{\text{Gal}} \simeq 8.34$ kpc) and extends toward the north Galactic pole in the first Galactic quadrant and toward the south Galactic pole in the third Galactic quadrant.

The standard deviation of the H II region sample shown in the bottom panel of Figure 4 is relatively constant in the inner Galaxy. The inner Galaxy values are all < 50 pc, and this can be thought of as the scale height. In the outer Galaxy, the standard deviation increases with Galactocentric radius as a result of the Galactic warp. This agrees with the results of the H II region study by Paladini et al. (2004) and the CO study by Malhotra (1994). We exclude R_{Gal} bins that have fewer than 10 sources from these computations.

In the analysis of the HMSF midplane (Section 4), we exclude sources with $R_{\text{Gal}} > R_0$, where $R_0 = 8.34$ kpc. We also exclude regions with distance uncertainties $> 50\%$. We show the Galactic locations of the H II regions studied here in Figure 5. The lack of regions within 10° of the Galactic Center is in part caused by a lack of known distances for those regions. Most regions in the

large concentration near $\ell = 80^\circ$ are associated with the Cygnus X complex.

3.1. Subsamples of the WISE Catalog

Due to issues of completeness and biases introduced by large H II region complexes, we define multiple subsamples of the WISE catalog. We run our analyses on these subsamples to investigate potential biases in our results. We also test the impact of using different rotation curve models. For all subsamples, we include only regions with $R_{\text{Gal}} < R_0$, with $R_0 = 8.34$ kpc.

3.1.1. Galactic Quadrants

The completeness of the WISE catalog varies across the Galaxy. Nearly all recent H II region surveys have taken place in the northern sky, and therefore there are many more known H II regions in the first Galactic quadrant compared to the fourth. The luminosity distribution of the first quadrant sample suggests that it is complete for all H II regions ionized by single O-stars, but this is not the case in the fourth quadrant (W. Armentrout et al., 2018, in prep.). This asymmetry may introduce a bias into our analysis. We therefore perform our analyses below using two Galactic longitude subsamples that both have $R_{\text{Gal}} < R_0$: one from $10^\circ < \ell < 75^\circ$ (hereafter the “first quadrant sample”) and one containing all regions in the first and fourth quadrants (the “inner Galaxy sample”). The first quadrant sample has 682 H II regions, 458 of which have known distances, and the inner Galaxy sample has 1149 H II regions, 613 of which have known distances.

3.1.2. H II Region Complexes

H II regions are frequently found in large complexes containing many individual H II regions. The WISE catalog lists entries for each individual region in the complex and therefore the results of a statistical study will differ based on whether the complex is considered to be one H II region or many. There are ~ 600 objects in the WISE catalog that do not have ionized gas or molecular spectroscopic observations, but are placed into a complex on the basis of the appearance of the complex in mid-infrared and radio continuum data (e.g., W49, W51, Sgr B2, etc.). The distance to these regions are assumed to be that of the other complex members. These large complexes may bias our results because there are many regions in the catalog at particular Galactic locations. This bias may be warranted because these large complexes may better define the midplane (as found by V. Cunningham et al., 2018, in prep.).

We test for the effect of complexes on our results by running the analyses on two subsamples, one only containing “unique” H II regions (i.e., each complex contains

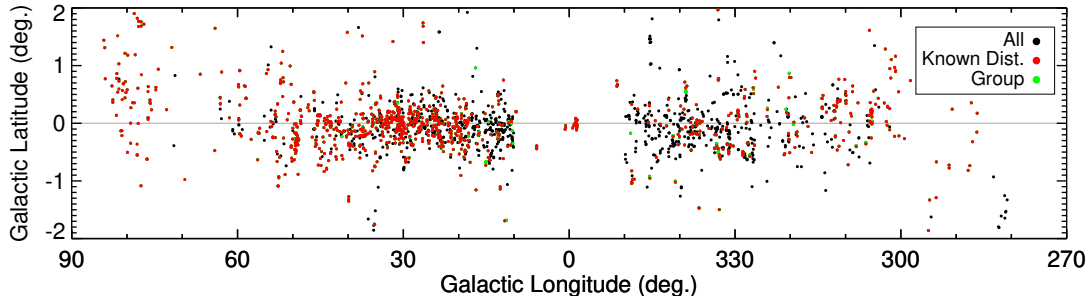


Figure 5. Galactic distribution of H II regions with $R_{\text{Gal}} < R_0$. Regions without known distances are shown as black dots, those with kinematic distances are shown with red dots, and the few “group” regions that are in large H II region complexes but which lack individual spectroscopic observations are shown with green dots. Unless they have trigonometric parallax distances or velocities consistent with the nuclear disk, sources within 10° of the Galactic Center lack known distances. The latitude range here is restricted to show greater detail, and this excludes some regions from the plot.

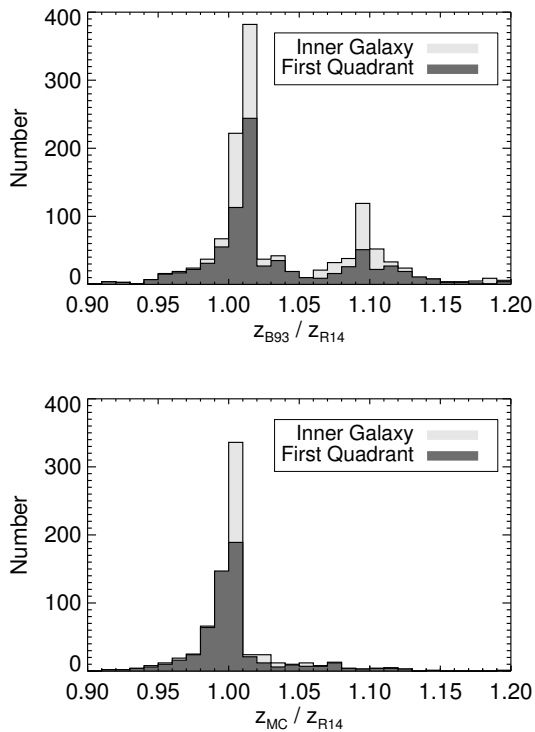


Figure 6. Distribution of z -heights for the B93, R14, and MC distances, expressed as a ratio. The B93 curve returns larger Heliocentric distances on average when compared with distances from the R14 curve and MC distances, and therefore on average has larger z heights. There is no significant difference between the inner Galaxy and first quadrant samples. The bi-modal distribution in the top panel is due to B93 distances being preferentially larger than R14 distances for a given source velocity if the source is nearby, but the two rotation curves giving similar distances otherwise. The larger uncertainties $z_{\text{B93}}/z_{\text{R14}} > 1.05$ are all from sources at the near kinematic distance. This, combined with the fact that the distances themselves are not evenly distributed gives rise to the bi-modal nature.

only one catalog entry), and the other that has all regions, including “group” regions that are in large H II region complexes but which lack individual spectroscopic observations. For the group regions, we assume the kinematic distance of the other complex members. We only show results from these subsamples in the first Galactic quadrant. In the first Galactic quadrant, the unique subsample contains 605 H II regions, 408 of which have known distances, and the group subsample contains 1132 H II regions, 725 of which have known distances.

3.1.3. Rotation Curves

The majority of the *WISE* catalog distances are kinematic, and are therefore sensitive to the choice of rotation curve. Different distances result in different values for z (cf. Equation 8). We examine how our results change when kinematic distances are computed using the B93 curve, the Reid et al. (2014, hereafter “R14”), and the MC analysis. We do not change the parallax distances in any of our trials. R14 lists multiple rotation curve models; the one we use here has a solar circular angular velocity $\Omega_0 = 235 \text{ km s}^{-1}$, a solar distance from the Galactic Center $R_0 = 8.34 \text{ kpc}$, and $\Omega(R_{\text{Gal}}) = \Omega_0 - 0.1 R_{\text{Gal}}$. In general, the B93 curve gives larger distances compared to the R14 curve, and therefore the B93 z -distances are larger than those of R14 (Figure 6, top panel). The MC and R14 curve z -distances are similar (Figure 6, bottom panel).

3.2. Characterizing the H II Region Vertical Distribution

We characterize the *WISE* catalog Galactic latitude distribution for all H II regions in the sample and the z -distribution for regions with known distances in Table 3. These analyses do not rely on the modified midplane definition in Section 2, but are comparable to those derived by previous authors in Table 1.

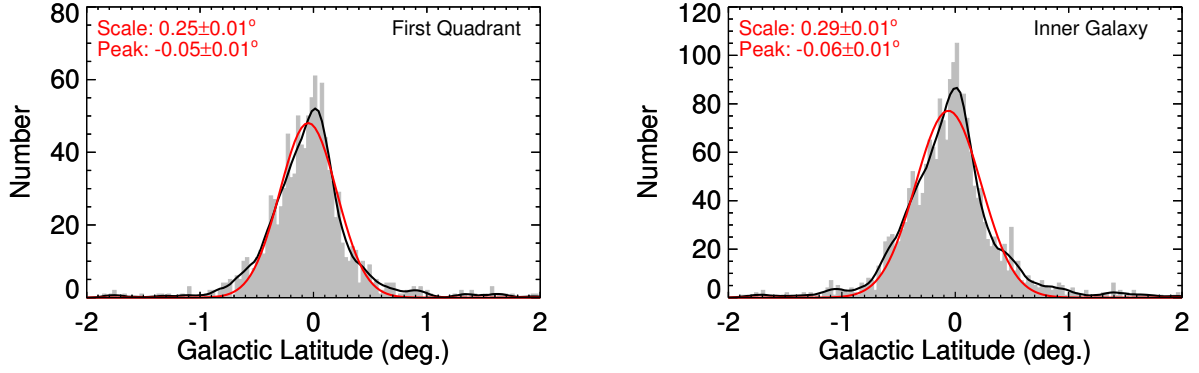


Figure 7. Galactic latitude distributions for H II regions in the first quadrant (left) and the inner Galaxy (right). The KDE is shown with a solid black curve, and this is fit with a Gaussian function shown as the red curve. The Gaussian fits to all subsamples peak at small negative values of b . That these distributions peak at negative latitudes can be explained if the Sun lies above the HMSF midplane. The scale heights from the Gaussian fits are all near 0.30° .

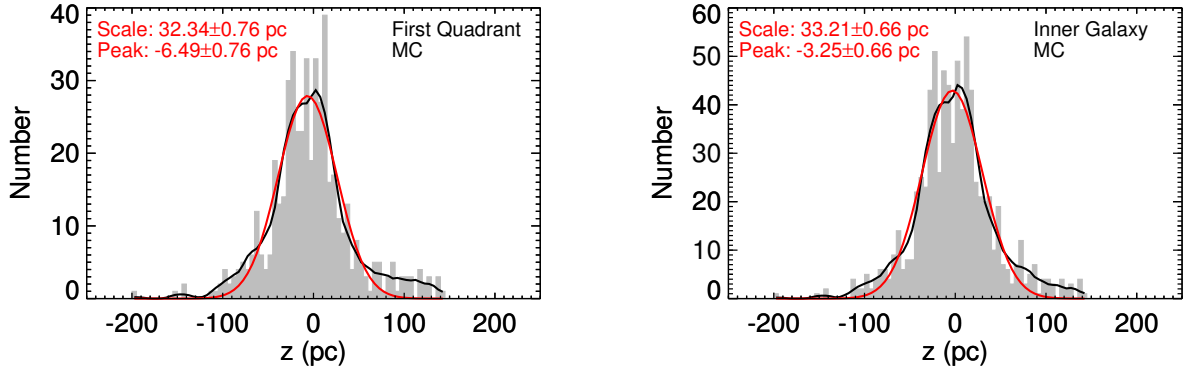


Figure 8. Height above the plane, z , for the first quadrant (left) and inner Galaxy samples (right) for MC distances. The KDE is shown with a solid black curve, and this is fit with a Gaussian function shown as the red curve. The Gaussian fits to the various subsamples peak at small negative values of z . That these distributions peak at negative z -heights can be explained if the Sun lies above the HMSF midplane.

Table 3. H II Region b and z -Distributions

Sample	Rot. Curve Modification	Galactic Latitude b			Height z		
		Number	Scale Height (deg.)	Peak (deg.)	Number	Scale Height (pc)	Peak (pc)
First Quadrant	MC	682	0.27 ± 0.01	-0.05 ± 0.01	458	32.3 ± 0.8	-6.5 ± 0.8
First Quadrant	MC	Unique	0.28 ± 0.01	-0.05 ± 0.01	408	33.5 ± 0.8	-6.2 ± 0.8
First Quadrant	MC	Group	0.29 ± 0.01	-0.05 ± 0.01	725	32.3 ± 0.8	-6.5 ± 0.8
First Quadrant	R14		0.27 ± 0.01	-0.05 ± 0.01	475	30.1 ± 0.8	-6.2 ± 0.8
First Quadrant	B93		0.27 ± 0.01	-0.05 ± 0.01	475	30.8 ± 0.8	-6.5 ± 0.8
Inner Galaxy	MC	1149	0.31 ± 0.01	-0.05 ± 0.01	613	33.2 ± 0.7	-3.2 ± 0.7
First Quadrant	MC	$r < 2$ pc	0.21 ± 0.01	-0.02 ± 0.01	104	24.4 ± 0.7	-4.6 ± 0.7
First Quadrant	MC	$2 < r < 5$ pc	0.34 ± 0.01	-0.04 ± 0.01	200	40.3 ± 1.1	-6.0 ± 1.1
First Quadrant	MC	$r > 5$ pc	0.29 ± 0.01	-0.07 ± 0.01	154	41.2 ± 0.9	-9.7 ± 0.9

3.2.1. Galactic Latitude Distribution

The distribution of Galactic latitudes is representative of the z -height distribution, but since it does not require distances to the objects the analysis can be done on a larger sample of H II regions. Figure 7 shows the first quadrant and inner Galaxy H II region Galactic latitude distributions, although we perform the same analysis for all subsamples defined previously, for all rotation curves. We plot the “kernel density estimation” (KDE) in the black curve. The KDE estimates the underlying distribution, and an analysis of the KDE is free from the uncertainties associated with the choice of bin size. For this and all subsequent analyses, we use the “Epanechnikov” kernel with the optimal bandwidth as suggested by Silverman (1986, their Equation 3.31). We fit the KDE distributions with Gaussian functions and store the results in Table 3.

For all subsamples, the peak of the Galactic latitude distribution is slightly below $b = 0^\circ$ (possibly indicating a positive value for the solar height z'_\odot), ranging from -0.04 to -0.06° . The scale height, again the standard deviation of a Gaussian fit to the Galactic latitude distribution, is between 0.25° and 0.30° for all subsamples. These scale height values are similar to those found for other high-mass star tracers (Table 1). It is interesting that our sample of H II regions, which spans a wide range of evolutionary stages, has the same scale height as tracers that are more sensitive to future star formation (e.g., sub-mm/mm clumps). We can infer that the lifetime of H II regions is short enough to not make a large difference in their b -distribution compared with younger objects.

3.2.2. z -Distribution

For regions with known distances, we can study the z -height distribution directly. The z -distributions, for which we show examples in Figure 8, are approximately Gaussian for all subsamples. There are, however, “wings” to the distributions at high and low values of z . As with the Galactic latitude distributions, we fit the KDEs of the z distributions with Gaussian functions and store the results in Table 3. The analysis of the z -distribution is necessarily limited to only H II regions with known distances, which is a smaller subsample compared to that used in the Galactic latitude analysis. All subsamples peak at small negative values, from -3 to -6 pc, again implying that the Sun is located above the midplane. The scale heights for the various subsamples range from 30 to 34 pc. All distance methods return similar results. These values are similar to those found for ultra-compact H II regions (Bronfman et al. 2000), sub-mm clumps (Wienen et al. 2015) and

high-mass star forming regions (Urquhart et al. 2011) (see Table 1).

3.2.3. Variations with HII Region Size

Finally, we test how the b - and z -distributions changes when the sample is restricted to H II regions of various physical sizes. The size of an H II region is a proxy for its age (e.g. Spitzer 1978). Diffuse H II regions are difficult to detect (Lockman et al. 1996; Anderson et al. 2017), and excluding larger diffuse regions from the sample may have an impact on the derived results. We divide the first quadrant sample into three physical size groups based on the *WISE* catalog radius r : $r < 2$ pc, $2 < r < 5$ pc, and $r > 5$ pc. We show these distributions and fits in Figure 9, and give the fit parameters in Table 3. Smaller regions have a smaller scale height of ~ 25 pc, whereas the largest regions have scale heights of ~ 40 pc. Furthermore, the larger region distributions are consistent with larger solar heights and hence larger tilt angles. Assuming the smaller regions are on average younger, this result is consistent with migration of older regions out of the plane as they age.

4. THE HMSF MIDPLANE DEFINED BY HII REGIONS

We use the results from Section 2 to define the HMSF midplane with H II regions. In this process, we determine the tilt and roll angles, and also the solar offset from the midplane. Our analysis necessarily ignores local deviations (e.g., Malhotra 1994, 1995) to find the average midplane definition most consistent with the data. As before, we exclude H II regions with $R_{\text{Gal}} > R_0$, H II regions within 10° in Galactic longitude of the Galactic Center, all regions with distance uncertainties $> 50\%$.

4.1. Midplane Tilt with $\theta_{\text{roll}} = 0^\circ$

We assume that the H II region z' distribution will peak at 0 pc for the “correct” value of z'_\odot . Changing z'_\odot alters z' for each H II region in the sample (Equation 5). This value of z'_\odot also results in a unique value for θ_{tilt} (Equation 7). With the limited number of fourth quadrant H II regions with known distances, θ_{roll} is difficult to constrain, and is often not accounted for in other analyses of the midplane (e.g., Goodman et al. 2014).

We vary z'_\odot from -30 pc to 40 pc in steps of 0.5 pc and recompute z' for all H II regions in the sample. For each distribution of z' values (for a given value of z'_\odot), we fit a Gaussian function to the KDE to determine the peak of the distribution (as in Figure 8). We show the values of the fitted Gaussian peaks as a function of z'_\odot and θ_{tilt} in Figure 10 and give the derived values of z'_\odot and θ_{tilt} in Table 4.

Table 4. HMSF Midplane Parameters

Sample	Rot. Curve	Modification	Number	$\theta_{\text{roll}} = 0^\circ$		$\theta_{\text{roll}} \text{ Free}$		
				z'_{\odot} (pc)	θ_{tilt} (deg.)	z'_{\odot} (pc)	θ_{tilt} (deg.)	θ_{roll} (deg.)
First Quadrant	MC		458	5.5 ± 2.5	-0.01 ± 0.01	5.6 ± 0.7	-0.01 ± 0.01	0.08 ± 0.01
First Quadrant	MC	Unique	408	4.5 ± 2.5	-0.02 ± 0.01	6.5 ± 0.8	0.00 ± 0.01	0.10 ± 0.01
First Quadrant	MC	Group	725	5.5 ± 2.5	-0.01 ± 0.01	9.4 ± 0.6	0.02 ± 0.01	0.11 ± 0.01
First Quadrant	R14		475	5.0 ± 2.5	-0.01 ± 0.01	4.2 ± 1.1	-0.02 ± 0.01	0.03 ± 0.01
First Quadrant	B93		475	5.5 ± 2.5	-0.01 ± 0.01	5.7 ± 1.2	-0.01 ± 0.01	0.04 ± 0.01
Inner Galaxy	MC		613	-2.8 ± 1.6	-0.07 ± 0.01	1.3 ± 0.4	-0.04 ± 0.01	0.04 ± 0.01
First Quadrant	MC	$d_{\text{cut}} = 4.7 \text{ kpc}, \alpha = -0.66$	306	4.8 ± 3.1	-0.01 ± 0.02
First Quadrant	MC	$ b < 0.5^\circ$	385	3.5 ± 2.5	-0.02 ± 0.02	15.0 ± 0.6	0.06 ± 0.01	0.05 ± 0.01
First Quadrant	MC	$ b < 1.0^\circ$	441	6.2 ± 1.6	0.00 ± 0.02	14.3 ± 0.7	0.05 ± 0.01	0.09 ± 0.01
First Quadrant	MC	$r < 2 \text{ pc}$	104	0.8 ± 1.6	-0.04 ± 0.01	-3.3 ± 1.3	-0.07 ± 0.01	-0.04 ± 0.01
First Quadrant	MC	$2 < r < 5 \text{ pc}$	200	3.5 ± 3.0	-0.02 ± 0.02	18.0 ± 1.2	0.08 ± 0.01	0.15 ± 0.01
First Quadrant	MC	$r > 5 \text{ pc}$	154	18.5 ± 3.5	0.08 ± 0.03	-8.6 ± 1.5	-0.11 ± 0.01	0.02 ± 0.01

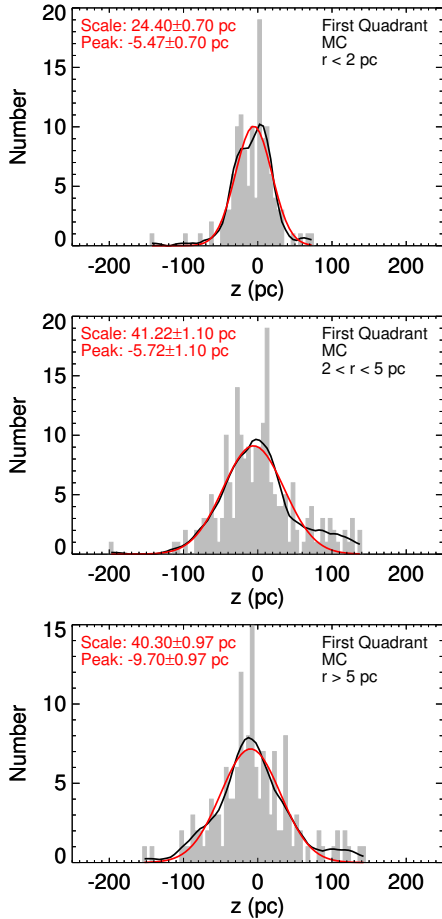


Figure 9. The z -distributions for small ($r < 2 \text{ pc}$; top), medium ($2 < r < 5 \text{ pc}$; middle), and large ($r > 5 \text{ pc}$; bottom) first quadrant HII region samples. The smallest regions have the narrowest distribution. The black lines are the KDEs and the red lines are Gaussian fits to the KDEs.

Our analysis finds that the Sun lies $\sim 5.6 \pm 2.6 \text{ pc}$ above the HMSF midplane for the first quadrant sample, for tilt angles of $\sim -0.01^\circ$, and $4.4 \pm 1.9 \text{ pc}$ below the plane for the inner Galaxy sample, for tilt angles of $\sim -0.07^\circ$. The uncertainties in the derived values of z'_{\odot} and θ_{tilt} come from allowing the peak to fall within the range $\pm 1 \text{ pc}$.

4.2. Midplane Tilt and Roll

Similar to our investigation of the midplane tilt, we can test for the midplane roll by fitting the distributions of z' for the HII region sample. For a one-dimensional fit, we cannot allow θ_{tilt} (or, equivalently, z'_{\odot}) and θ_{roll} to both be free parameters. Instead, we set θ_{roll} to a range of discrete values, and fit for θ_{tilt} .

We compute a grid of z' distributions for θ_{roll} values from -0.8 to 0.2° in increments of 0.05° . We then vary z'_{\odot} (and hence θ_{tilt}) as in Section 4.1 until we find the combination of θ_{tilt} and θ_{roll} where the z' distribution of HII regions peaks at 0 pc . We show the combinations of θ_{tilt} and θ_{roll} that together lead to distributions peaking at $z' = 0$ in Figure 11 for the first quadrant and inner Galaxy samples. There is a negative correlation between θ_{tilt} and θ_{roll} , such that increasing either angle has the same effect on the HII region distribution. From this one-dimensional analysis we cannot determine the best combination of the two angles, but we can constrain one angle given the other one.

4.3. Three-Dimensional Fit for Midplane Tilt and Roll

Instead of testing discrete values of θ_{tilt} and θ_{roll} by fitting the one-dimensional distribution of z' for HII regions, we can also simply fit a plane of the form in Equation 2 to the HII region distribution. In this way, we simultaneously fit for the Sun's height and the two midplane rotation angles. The downsides to this

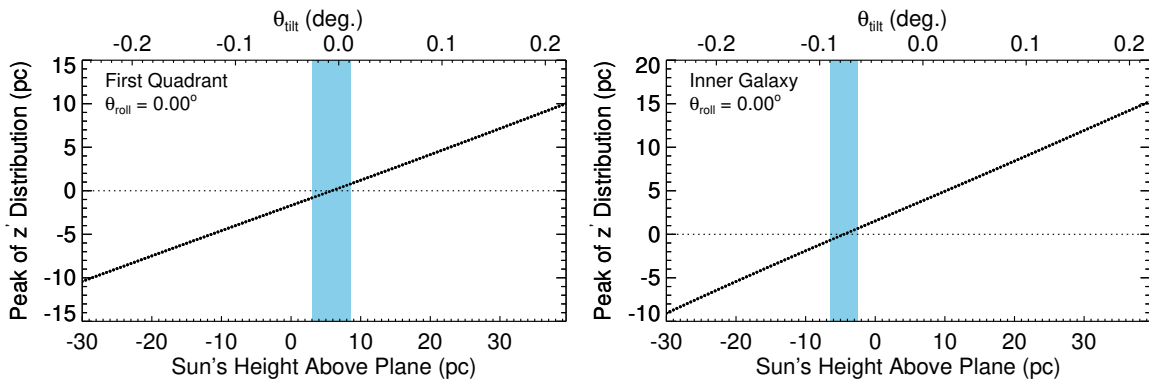


Figure 10. Peak of the H II region distribution as a function of solar height above the plane, z'_{\odot} for the first quadrant (left) and inner Galaxy (right) samples. The intersection of the blue shaded region with the x-axis shows values of z'_{\odot} that result in H II region distributions that peak from -1 to 1 pc.

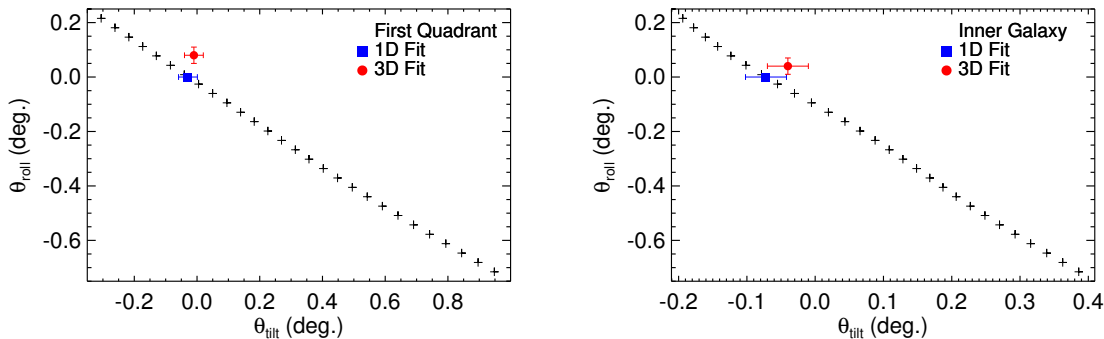


Figure 11. Variations in θ_{roll} as a function of θ_{tilt} for the first quadrant (left) and inner Galaxy (right) samples. Each point corresponds to the two tilt angles where the z' -distribution of H II regions is centered at zero. There is a negative correlation between the two angles. Blue squares show the values of θ_{tilt} we derived from one-dimensional fits with $\theta_{\text{roll}} = 0$, whereas the red circles indicate results from three-dimensional fits explained later in Section 4.3. Error bars are 3σ .

method are that it is difficult to compare with the one-dimensional fits frequently done by previous authors, and may produce results inconsistent with those of the one-dimensional fits.

We fit the plane using a robust least-squares minimization routine. The robust least squares fit reduces the impact of outliers on the fit results by minimizing the “loss function,” $\rho(z)$, where z is the squared residuals. We use a “soft l1” loss function, $\rho(z) = \sqrt{1 + z^2} - 1$, which is similar to the “Huber” loss function. As before, we force the plane to pass through the location of Sgr A*. We perform these three-dimensional fits for the same subsamples as the one-dimensional fits and store the results in the final three columns of Table 4.

The results from the three-dimensional fits are similar to those found previously in the one-dimensional fits, despite allowing for a second midplane tilt angle. We find small absolute tilt angles and small positive values for the Solar height about the plane. In the first quadrant sample, for example, $\theta_{\text{tilt}} = -0.01^\circ$ and $z'_{\odot} = 5.7$. The

roll angle is generally small as well, and almost always positive; $\theta_{\text{roll}} = 0.08^\circ$ for the first quadrant sample and $\theta_{\text{roll}} = -0.04^\circ$ for the inner Galaxy sample. As can be seen in Figure 11, the values of θ_{tilt} and θ_{roll} derived from the three-dimensional fits are broadly consistent ($\sim 5\sigma$) with the one-dimensional relationships. This gives us additional confidence in the derived values.

4.4. Effects of Completeness and Latitude Restrictions

Since the *WISE* catalog contains a greater quantity of extremely distant sources compared with other catalogs of star formation regions, we here examine if our results would change if the sample were less complete.

4.4.1. Artificial Distance Cutoff

As a first test, we restrict our first quadrant sample by removing sources above a range of Heliocentric distances from 1.75 to 8.25 kpc. We then fit the KDE distributions of these restricted samples with Gaussians as before, and show the results in Figure 12. We see in this figure that the peak of the z distributions varies from

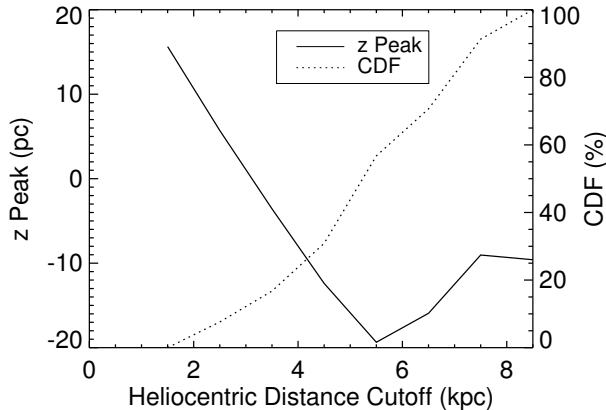


Figure 12. Variations in the peak of H II region distributions restricted by Heliocentric distance cutoffs from 1.75 to 8.25 pc (solid curve). Also shown is the cumulative distribution function for the H II region sample unrestricted by distance (dotted curve). Imposing a distance cutoff changes the derived z -distribution peak from -20 to $+15$ pc.

-19 pc to $+17$ pc. This simple analysis shows that an artificial distance cutoff may have a significant effect on the derived values.

4.4.2. Malmquist Bias

A flux-limited distribution of course does not have a hard distance cutoff. We attempt to model a more accurate Malmquist bias by comparing the H II region distance distribution to that of another flux-limited sample. We choose to do the comparison with the Bolocam Galactic Plane Survey (BGPS) catalog (Ellsworth-Bowers et al. 2015), although any flux-limited sample could serve the same purpose.

The BGPS catalog contains 3508 mm clumps, 1710 of which have kinematic distances. In the first quadrant zone $10^\circ < \ell < 75^\circ$, there are 2843 clumps identified from mm-wave observations, 1214 of which have kinematic distances. The distribution of BGPS Heliocentric distances differs from that of the *WISE* H II regions in that it has a stronger peak near 5 kpc and a steeper decrease thereafter (see below). This indicates that there is either an asymmetry in the mm-clump/H II region ratio or that there is Malmquist bias in the subset of BGPS sources with known distances.

We attempt to evaluate the impact of potential Malmquist bias by applying a source removal function to the H II region sample that more closely approximates the effects of Malmquist bias. We create a modified H II region distribution by keeping all sources in the catalog that have Heliocentric distances less than a cutoff distance d_{cut} . For sources with distances greater than the cutoff value, we apply a power law source removal function with a power law index α . The percent likelihood

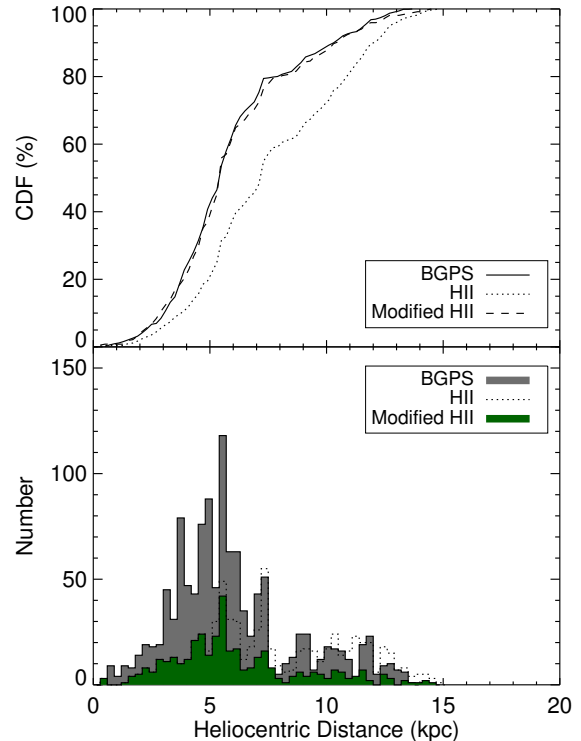


Figure 13. First-quadrant distributions of Heliocentric distances for the BGPS and H II region samples. Since the BGPS catalog is limited to within $|b| < 0.5^\circ$ in the first quadrant, we also show the H II region distribution with this limitation. The BGPS distribution is heavily weighted toward relatively nearby sources compared to the H II region distribution.

that a source with a Heliocentric distance d is kept in the catalog is therefore:

$$p = \begin{cases} 1, & \text{if } d < d_{\text{cut}} \\ (d_{\odot} - d_{\text{cut}})^{-\alpha}, & \text{if } d \geq d_{\text{cut}}. \end{cases} \quad (9)$$

We iterate d_{cut} and α in the respective ranges 0 to 12 kpc and 0 to 1 to create modified H II region distributions, and perform a Kolmogorov-Smirnov (K-S) test on the BGPS and modified H II region distributions. The K-S test can determine the likelihood that two samples are drawn from the same parent distribution.

We find that the two distributions are most similar when $\alpha = -0.66$ and $d_{\text{cut}} = 4.7$ kpc. We show the Heliocentric distance cumulative distribution functions (CDFs) before and after the modification in Figure 13, top panel, and the distributions themselves in Figure 13, bottom panel.

Fitting this modified H II region distribution using one-dimensional fits as in Section 3 does impact the derived parameters, although the fits to the modified distribution give similar peaks and scale heights as are

found for the complete distribution. Repeating the Sun’s height analysis, we find that the modified H II region distribution is consistent with the Sun lying 12.5 pc above the midplane, for a tilt angle $\theta_{\text{tilt}} = 0.04^\circ$. These values are considerably larger than the unmodified values of 5.5 pc and $\theta_{\text{tilt}} = -0.01^\circ$. We conclude that Malmquist bias can significantly alter the derived values of the Galactic midplane.

4.4.3. Latitude Restrictions

Most surveys of the Galactic plane are restricted in latitude. For example, the BGPS was limited to $|b| < 0.5^\circ$. When creating the *WISE* catalog, we searched *WISE* data within 8° of the plane, but included known regions outside this range. The *WISE* catalog therefore is more complete in latitude compared with catalogs derived from most other Galactic plane surveys. To test the effect of this latitude limitation, we restrict our first-quadrant sample to within $|b| < 0.5^\circ$ and $|b| < 1.0^\circ$ and repeat the above analyses. We again find the peak and scale height are essentially unchanged. The solar height is 3.0 pc for $|b| < 0.5^\circ$ and 6.5 pc for $|b| < 1.0^\circ$, for tilt angles $\theta_{\text{tilt}} = -0.03^\circ$ and $\theta_{\text{tilt}} = 0.00^\circ$, respectively. The former values are considerably different from the unrestricted values of 5.8 pc and $\theta_{\text{tilt}} = -0.01^\circ$. Therefore, restricting the sample to within $|b| < 0.5^\circ$ significantly changes our results, but there is no such effect if limited to $|b| < 1.0^\circ$. We conclude that surveys with $|b| < 1.0^\circ$ can reproduce the z -distribution results from our more complete sample, but surveys with $|b| < 0.5^\circ$ cannot.

5. SUMMARY

We developed a framework for studies of the Galactic midplane, assuming that the midplane passes through the location of Sgr A*. We allowed for rotation of the midplane about Galactic azimuths of 90° (the “tilt”; θ_{tilt}) and 0° (the “roll”; θ_{roll}). Our framework can be applied to any sample of Galactic objects to determine the midplane, thereby determining the tilt and roll angles with respect to the current midplane definition and also the Sun’s height above the midplane.

We applied this framework to the *WISE* Catalog of Galactic H II Regions to define the high-mass star formation (HMSF) midplane. In other work (Armentrout et al., 2018, in prep.), we have found that the *WISE* catalog is statistically complete for all first-quadrant H II regions ionized by single O-stars, giving us a volume-limited sample. The fourth quadrant sample is less complete, and we therefore analyze the first quadrant and inner Galaxy (first and fourth quadrants) samples independently. We computed a Galactic latitude H II region scale height of $\sim 0.30^\circ$, and a z -distribution scale height

of ~ 30 pc. These values are dependent on the size of the H II regions themselves. The smallest H II regions (< 2 pc radius) have the smallest scale height distribution of 26 pc. Larger H II regions have a scale height of ~ 40 pc. Since the size of an H II region depends on its age, these results may indicate a broadening of the H II region distribution as the regions themselves evolve.

We found that the HMSF midplane is not significantly different from the current IAU midplane, and that the Sun is near to the HMSF midplane. Values for the first quadrant and inner Galaxy samples are similar, although the first quadrant sample analysis supports a solar height of ~ 5 pc above the current midplane and the inner Galaxy sample analysis supports a solar height of a few pc below the current midplane. The tilt and roll angles as defined here are negatively correlated, although when θ_{roll} is a free parameter we find similar values for θ_{tilt} and the solar height as when θ_{roll} is set to zero. We caution that the roll angle is not well-constrained due to a lack of H II regions with known distances in the fourth Galactic quadrant.

Our values for the solar height are ~ 15 pc less than those found in studies of stars, but they are consistent with many results of HMSF tracers. The meaning of this discrepancy is unclear. The stellar samples are compiled over a different portion of the Galaxy compared to ours, since extinction drastically limits the distance stars can be seen in the midplane. The discrepancy between our results may indicate that near to the Sun there is a large-scale displacement in the stellar population. Since many of the stellar studies rely on counting stars toward the north and south Galactic poles, asymmetries in the stellar distribution would alter the derived result for the solar height. For example, Xu et al. (2015) discovered an asymmetry in the main-sequence star counts using data from the Sloan Digital Sky Survey such that there are more stars in the north 2 kpc from the Sun, more stars in the south between 4–6 kpc from the Sun, and more stars in the north between 8–10 kpc from the Sun. Such asymmetries may make determinations of the solar height difficult using star counts.

Our values are, however, broadly consistent with the results of Wegg et al. (2015). They found from near-infrared star counts of red clump giants that the mean latitude in the Galactic long bar is $b \simeq -0.1^\circ$ and that the long bar lies in the midplane after accounting for the midplane tilt. At a longitude of the end of the long bar of $\ell \simeq 30^\circ$, a distance of 6000 kpc, $b = -0.10^\circ$, $\theta_{\text{tilt}} = -0.01^\circ$, and $\theta_{\text{roll}} = 0^\circ$, $z' \simeq -4$ pc. If we redo the calculation with the first-quadrant sample values of $\theta_{\text{tilt}} = -0.01^\circ$ and $\theta_{\text{roll}} = 0.08^\circ$, $z' \simeq -0.1$ pc, which implies that the long bar is exactly in the modified mid-

plane. Using the inner Galaxy values of $\theta_{\text{tilt}} = -0.04^\circ$ and $\theta_{\text{roll}} = 0.04^\circ$, $z' \simeq -4$ pc.

We tested the robustness of these results and applicability of our methodology using various permutations of our sample. Since most Galactic plane surveys are restricted in latitude, we examine H II region samples restricted to within $|b| < 1.0^\circ$ and $|b| < 0.5^\circ$. We found that the $|b| < 0.5^\circ$ sample results are considerably different, indicating that similar studies of the Milky Way vertical distribution should ideally not include a latitude restriction, and certainly cannot be limited to $|b| < 0.5^\circ$. Introducing an artificial Malmquist bias also changes the results significantly.

This work is supported by NSF grant AST1516021 to LDA. TMB acknowledges support from NSF grant AST 1714688. Support for TVW was provided by the NSF through the Grote Reber Fellowship Program administered by Associated Universities, Inc./National Radio Astronomy Observatory. We thank Bob Benjamin for enlightening discussions on early drafts of this manuscript. We thank Virginia Cunningham for help on early analyses for this project. The Green Bank Observatory and the National Radio Astronomy Observatory are facilities of the National Science Foundation operated under cooperative agreement by Associated Universities, Inc.

REFERENCES

- Anderson, L. D., Armentrout, W. P., Johnstone, B. M., et al. 2015, *ApJS*, 221, 26
- Anderson, L. D., Armentrout, W. P., Luisi, M., et al. 2017, ArXiv e-prints, arXiv:1710.07397
- Anderson, L. D., & Bania, T. M. 2009, *ApJ*, 690, 706
- Anderson, L. D., Bania, T. M., Balsaer, D. S., et al. 2014, *ApJS*, 212, 1
- Becker, R. H., White, R. L., Helfand, D. J., & Zoonematkermani, S. 1994, *ApJS*, 91, 347
- Beichman, C. A., Neugebauer, G., Habing, H. J., Clegg, P. E., & Chester, T. J., eds. 1988, *Infrared astronomical satellite (IRAS) catalogs and atlases. Volume 1: Explanatory supplement, Vol. 1*
- Beuther, H., Tackenberg, J., Linz, H., et al. 2012, *ApJ*, 747, 43
- Blaauw, A., Gum, C. S., Pawsey, J. L., & Westerhout, G. 1960, *MNRAS*, 121, 123
- Bobylev, V. V., & Bajkova, A. T. 2016, ArXiv e-prints, arXiv:1601.06741
- Brand, J. 1986, PhD thesis, Leiden Univ., Netherlands.
- Brand, J., & Blitz, L. 1993, *A&A*, 275, 67
- Bronfman, L., Casassus, S., May, J., & Nyman, L.-Å. 2000, *A&A*, 358, 521
- Chen, B., Stoughton, C., Smith, J. A., et al. 2001, *ApJ*, 553, 184
- Clemens, D. P., Sanders, D. B., & Scoville, N. Z. 1988, *ApJ*, 327, 139
- Dame, T. M., Ungerechts, H., Cohen, R. S., et al. 1987, *ApJ*, 322, 706
- Ellsworth-Bowers, T. P., Rosolowsky, E., Glenn, J., et al. 2015, *ApJ*, 799, 29
- Ellsworth-Bowers, T. P., Glenn, J., Rosolowsky, E., et al. 2013, *ApJ*, 770, 39
- Goodman, A. A., Alves, J., Beaumont, C. N., et al. 2014, *ApJ*, 797, 53
- Humphreys, R. M., & Larsen, J. A. 1995, *AJ*, 110, 2183
- Jurić, M., Ivezić, Ž., Brooks, A., et al. 2008, *ApJ*, 673, 864
- Kalberla, P. M. W. 2003, *ApJ*, 588, 805
- Karim, M. T., & Mamajek, E. E. 2017, *MNRAS*, 465, 472
- Langer, W. D., Pineda, J. L., & Velusamy, T. 2014, *A&A*, 564, A101
- Lockman, F. J., Pisano, D. J., & Howard, G. J. 1996, *ApJ*, 472, 173
- Maíz-Apellániz, J. 2001, *AJ*, 121, 2737
- Malhotra, S. 1994, *ApJ*, 433, 687
- . 1995, *ApJ*, 448, 138
- Mercer, E. P., Clemens, D. P., Meade, M. R., et al. 2005, *ApJ*, 635, 560
- Molinari, S., Noriega-Crespo, A., Bally, J., et al. 2015, ArXiv e-prints, arXiv:1511.06300
- Paladini, R., Burigana, C., Davies, R. D., et al. 2003, *A&A*, 397, 213
- Paladini, R., Davies, R. D., & DeZotti, G. 2004, *MNRAS*, 347, 237
- Reid, M. J., & Brunthaler, A. 2004, *ApJ*, 616, 872
- Reid, M. J., Menten, K. M., Zheng, X. W., et al. 2009, *ApJ*, 700, 137
- Reid, M. J., Menten, K. M., Brunthaler, A., et al. 2014, *ApJ*, 783, 130
- Rosolowsky, E., Dunham, M. K., Ginsburg, A., et al. 2010, *ApJS*, 188, 123
- Silverman, B. W. 1986, *Density estimation for statistics and data analysis*
- Spitzer, L. 1978, *Physical processes in the interstellar medium*, ed. Spitzer, L.
- Urquhart, J. S., Morgan, L. K., Figura, C. C., et al. 2011, *MNRAS*, 418, 1689
- van Tulder, J. J. M. 1942, *BAN*, 9, 315
- Walsh, A. J., Hyland, A. R., Robinson, G., & Burton, M. G. 1997, *MNRAS*, 291, 261
- Wegg, C., Gerhard, O., & Portail, M. 2015, *MNRAS*, 450, 4050
- Wenger, T. V., Balsaer, D. S., Anderson, L. D., & Bania, T. M. 2018, *ApJ*, 856, 52
- Wienen, M., Wyrowski, F., Menten, K. M., et al. 2015, *A&A*, 579, A91
- Wood, D. O. S., & Churchwell, E. 1989, *ApJS*, 69, 831
- Xu, Y., Newberg, H. J., Carlin, J. L., et al. 2015, *ApJ*, 801, 105

APPENDIX

A. COORDINATE CONVERSIONS

Ellsworth-Bowers et al. (2013) derived the relationship between Galactic positions measured from the current coordinate system that uses the IAU standards and the values measured from the modified Galactic plane. Their derived relationship did not consider the offset of Sgr A* from $(\ell, b) = (0^\circ, 0^\circ)$ or the roll of the plane, and we update their calculations with these changes.

In our nomenclature, unprimed coordinates refer to the values in the currently-defined Sun-centered coordinate system and primed values refer to the Sgr A*-centered values that include the tilt and roll of the midplane. See Figures 1, 2, and 3 for images of the various distances and angles.

For local Cartesian coordinates with the Sun at the origin, the current IAU definition gives:

$$\begin{pmatrix} x \\ y \\ z \end{pmatrix} = \begin{pmatrix} d_\odot \cos \ell \cos b \\ d_\odot \sin \ell \cos b \\ d_\odot \sin b \end{pmatrix}, \quad (\text{A1})$$

where \hat{x} points from the Sun to the Galactic Center, \hat{y} is in the Galactic plane and points toward a Galactic azimuth of 90° , and \hat{z} points toward the north Galactic pole.

The location of Sgr A* is $(\ell_{\text{SgrA*}}, b_{\text{SgrA*}}) = (359.944249, -0.046165^\circ)$ (Reid & Brunthaler 2004), so

$$y_{\text{SgrA*}} = R_0 \sin \ell_{\text{SgrA*}}. \quad (\text{A2})$$

and

$$z_{\text{SgrA*}} = R_0 \sin b_{\text{SgrA*}}. \quad (\text{A3})$$

The tilt angle between the currently-defined Galactic midplane and the modified plane is:

$$\theta_{\text{tilt}} = \sin^{-1} \left(\frac{z'_\odot + z_{\text{SgrA*}}}{R_0} \right). \quad (\text{A4})$$

This differs from the angle used in Ellsworth-Bowers et al. (2013) by the additional term $z_{\text{SgrA*}}$. Note that $z_{\text{SgrA*}}$ is negative for $b_{\text{SgrA*}} < 0$.

The full translational and rotational matrices resulting from (1) rotating about the \hat{z} -axis so that \hat{x} points toward the Sun, (2) moving the origin to be centered on Sgr A*, (3) rotating about the \hat{z} -axis by the angle $360^\circ - \ell_{\text{SgrA*}}$ (or, equivalently, clockwise by $\ell_{\text{SgrA*}}$) so that \hat{x}' points toward the Sun, (4) rotating the Galactic plane about the \hat{y} -axis (with the Sun at the origin) clockwise by the angle θ_{tilt} , and (5) rotating the Galactic plane counterclockwise about the \hat{x} -axis by the angle θ_{roll} :

$$\begin{pmatrix} x' \\ y' \\ z' \\ 1 \end{pmatrix} = \begin{pmatrix} 1 & 0 & 0 & 0 \\ 0 & \cos \theta_{\text{roll}} & \sin \theta_{\text{roll}} & 0 \\ 0 & -\sin \theta_{\text{roll}} & \cos \theta_{\text{roll}} & 0 \\ 0 & 0 & 0 & 1 \end{pmatrix} \begin{pmatrix} \cos \theta_{\text{tilt}} & 0 & -\sin \theta_{\text{tilt}} & 0 \\ 0 & 1 & 0 & 0 \\ \sin \theta_{\text{tilt}} & 0 & \cos \theta_{\text{tilt}} & 0 \\ 0 & 0 & 0 & 1 \end{pmatrix} \begin{pmatrix} \cos \ell_{\text{SgrA*}} & \sin \ell_{\text{SgrA*}} & 0 & 0 \\ -\sin \ell_{\text{SgrA*}} & \cos \ell_{\text{SgrA*}} & 0 & 0 \\ 0 & 0 & 1 & 0 \\ 0 & 0 & 0 & 1 \end{pmatrix} \begin{pmatrix} 1 & 0 & 0 \\ 0 & 1 & 0 \\ 0 & 0 & 1 \end{pmatrix} \begin{pmatrix} -1 & 0 & 0 \\ 0 & -1 & 0 \\ 0 & 0 & 1 \end{pmatrix} \begin{pmatrix} x \\ y \\ z \\ 1 \end{pmatrix}.$$

Although the tilt rotation is defined in reference to the current midplane definition (a rotation centered on the Sun), the roll is defined from the tilted modified midplane (a rotation centered on Sgr A*). The derived coordinates are therefore:

$$\begin{pmatrix} x' \\ y' \\ z' \end{pmatrix} = \begin{pmatrix} (R_0 - x) \cos \ell_{\text{SgrA*}} \cos \theta_{\text{tilt}} + (y_{\text{SgrA*}} - y) \sin \ell_{\text{SgrA*}} \cos \theta_{\text{tilt}} - (z - z_{\text{SgrA*}}) \sin \theta_{\text{tilt}} \\ (R_0 - x) (\sin \ell_{\text{SgrA*}} \cos \theta_{\text{roll}} + \cos \ell_{\text{SgrA*}} \sin \theta_{\text{roll}} \sin \theta_{\text{tilt}}) - (y_{\text{SgrA*}} - y) (\cos \ell_{\text{SgrA*}} \cos \theta_{\text{roll}} - \sin \theta_{\text{tilt}} \sin \theta_{\text{roll}}) + (z - z_{\text{SgrA*}}) \cos \theta_{\text{tilt}} \sin \theta_{\text{roll}} \\ (R_0 - x) (\sin \ell_{\text{SgrA*}} \sin \theta_{\text{roll}} - \cos \ell_{\text{SgrA*}} \sin \theta_{\text{tilt}} \cos \theta_{\text{roll}}) + (y_{\text{SgrA*}} - y) (\sin \ell_{\text{SgrA*}} \cos \theta_{\text{roll}} \sin \theta_{\text{tilt}} + \cos \ell_{\text{SgrA*}} \sin \theta_{\text{roll}}) + (z - z_{\text{SgrA*}}) \cos \theta_{\text{tilt}} \cos \theta_{\text{roll}} \end{pmatrix}. \quad (\text{A5})$$

Since $\sin(\ell_{\text{SgrA}^*}) = -0.0009730 \simeq 0$ and $\cos(\ell_{\text{SgrA}^*}) = 0.9999995 \simeq 1$, these reduce to

$$\begin{pmatrix} x' \\ y' \\ z' \end{pmatrix} = \begin{pmatrix} (R_0 - x) \cos \theta_{\text{tilt}} - (z - z_{\text{SgrA}^*}) \sin \theta_{\text{tilt}} \\ (R_0 - x) \sin \theta_{\text{tilt}} \sin \theta_{\text{roll}} + (y_{\text{SgrA}^*} - y) \cos \theta_{\text{roll}} + (z - z_{\text{SgrA}^*}) \cos \theta_{\text{tilt}} \sin \theta_{\text{roll}} \\ (R_0 - x) \sin \theta_{\text{tilt}} \cos \theta_{\text{roll}} - (y_{\text{SgrA}^*} - y) \sin \theta_{\text{roll}} + (z - z_{\text{SgrA}^*}) \cos \theta_{\text{tilt}} \cos \theta_{\text{roll}} \end{pmatrix}. \quad (\text{A6})$$

Since x and y are of order $\sim \text{kpc}$ and because θ_{tilt} and θ_{roll} are both small, rotations of the midplane will have a larger fractional affect on derived values in z' compared to x' and y' . In the limit that $\theta_{\text{roll}} = 0$,

$$\begin{pmatrix} x' \\ y' \\ z' \end{pmatrix} = \begin{pmatrix} (R_0 - x) \cos \theta_{\text{tilt}} - (z - z_{\text{SgrA}^*}) \sin \theta_{\text{tilt}} \\ y_{\text{SgrA}^*} - y \\ (R_0 - x) \sin \theta_{\text{tilt}} + (z - z_{\text{SgrA}^*}) \cos \theta_{\text{tilt}} \end{pmatrix}. \quad (\text{A7})$$

These expressions differ from those in [Ellsworth-Bowers et al. \(2013\)](#) by the additional y_{SgrA^*} and z_{SgrA^*} terms.